



The space telescope NINA: results of a beam test calibration

V. Bidoli^a, M. Casolino^a, M.P. De Pascale^a, A. Morselli^a, G. Furano^a, P. Picozza^a,
A. Scoscini^a, R. Sparvoli^{a,*}, G. Barbiellini^b, W. Bonvicini^b, R. Cirami^b,
P. Schiavon^b, A. Vacchi^b, N. Zampa^b, M. Ambriola^c, R. Bellotti^c, F. Cafagna^c, F. Ciacio^c,
M. Castellano^c, M. Circella^c, C. De Marzo^c, S. Bartalucci^d, S. Giuntoli^d, M. Ricci^d,
P. Papini^e, S. Piccardi^e, P. Spillantini^e, A. Bakaldin^f, A. Batishev^f, A.M. Galper^f,
S. Koldashov^f, M. Korotkov^f, V. Mikhailov^f, A. Murashov^f, S. Voronov^f, M. Boezio^g

^a *Department of Physics, University of Rome "Tor Vergata" and INFN Via della Ricerca Scientifica 1, 00133 Rome, Italy*

^b *University of Trieste and INFN Section of Trieste, Trieste, Italy*

^c *University of Bari and INFN Section of Bari, Bari, Italy*

^d *INFN Laboratori Nazionali di Frascati, Frascati, Italy*

^e *University of Firenze and INFN Section of Firenze, Firenze, Italy*

^f *Moscow Engineering Physics Institute, Moscow, Russia*

^g *Royal Institute of Technology, Stockholm, Sweden*

Received 9 June 1998

Abstract

In June 1998 the telescope NINA will be launched in space on board of the Russian satellite Resource-01 n.4. The main scientific objective of the mission is the study of the anomalous, galactic and solar components of the cosmic rays in the energy interval 10–200 MeV/n. The core of the instrument is a silicon detector whose performances have been tested with a particle beam at the GSI Laboratory in Germany in 1997; we report here on the results obtained during the beam calibration. © 1999 Elsevier Science B.V. All rights reserved.

PACS: 90; 95; 96; 98

Keywords: Cosmic rays; Isotopic composition; Satellite; Silicon detector; Beam test

1. Introduction

Starting from 1994, the Italian National Institute of Nuclear Physics (INFN) and the Moscow Engineering Physics Institute (MEPhI) have established a collaboration and conceived the Russian–Italian

Missions (RIM). They consist of four different experiments, one to be performed on board of the MIR space station (experiment SilEye [1]), and the other three onboard Russian satellites (experiments NINA, PAMELA [2] and GILDA [3]), dedicated to cosmic ray investigations in an energy spectrum extending for about 4 orders of magnitude (from 10 to 10⁵ MeV/n).

*Corresponding author.

The first of the RIM missions on satellite is NINA (a New Instrument for Nuclear Analysis); its goal is to detect cosmic ray nuclei of galactic, solar or anomalous origin, from hydrogen to iron, between 10 and 200 MeV/n [4]. The experiment will be carried out on board of the satellite Resource-01 n.4, developed by the Russian Space Company VNIIEM. The spacecraft will be launched on a polar orbit at 840 km of altitude in June 1998, for a three year long mission.

2. The instrument NINA

NINA, at present installed on the satellite as shown in Fig. 1, is divided in the following four subsystems:

- *Detector* (Box D1): it is composed of 32 silicon layers and the electronics for signal processing.
- *On-board computer* (Box D2): it is a dual micro-processor dedicated to data processing and to the selection of the trigger and the acquisition mode configuration.

- *Interface computer* (Box E): it rearranges the data coming from D2 and delivers them to the satellite telemetry system.
- *Power supply* (Box P): it distributes the power supply to the different subsystems.

Such an organization of the detector allowed to independently build and test the different subsystems, simplifying in this way the construction and integration process. The weight and electric power of the complete telescope are respectively 40 kg and 40 W, in accordance with the constraints imposed by the satellite. To safeguard from possible malfunctions and breakings, a global redundancy of every electronic system has been implemented in NINA.

Following the usual satellite mission procedures, NINA has already been built in two versions: an Engineering Model, used for all functionality tests and compatibility operations with the satellite, and a Flight Model, equal to the previous one, ready to fly.

2.1. The silicon detector

The active part of the NINA instrument is a telescope composed of 16 X–Y planes, giving information on the energy of the crossing particle and its incident angle. The sensitive element consists of two n-type silicon detectors, $60 \times 60 \text{ mm}^2$, each divided in 16 strips and attached to a supporting ceramic frame passing under the lateral strips 1 and 16. The couple of detectors is mounted with the strips right-angled, in order to measure the X and Y coordinates of the particle. The thickness of the first pair is $150 \pm 15 \mu\text{m}$; all the others, instead, are $380 \pm 15 \mu\text{m}$ thick, for a total thickness of 11.7 mm of silicon [5,6]; the indetermination is due to the process of manufacturing.

The lateral strips (nos. 1 and 16) are used for the anticoincidence system (AC) and are read together by the same electronic channel, except for the plane 1 where they are physically disconnected.

A photograph of the whole detector is shown in Fig. 2. Each plane with its electronics is mounted on an aluminum frame; interplanar distance is 1.4 cm, except for the first and second planes separated by 8.5 cm, for a better measurement of the

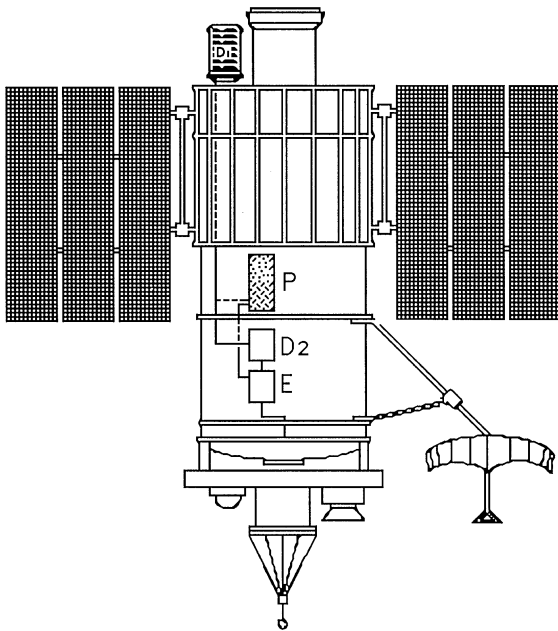


Fig. 1. Positioning of the various systems of NINA – D1, D2, E and P – onto the satellite resource.

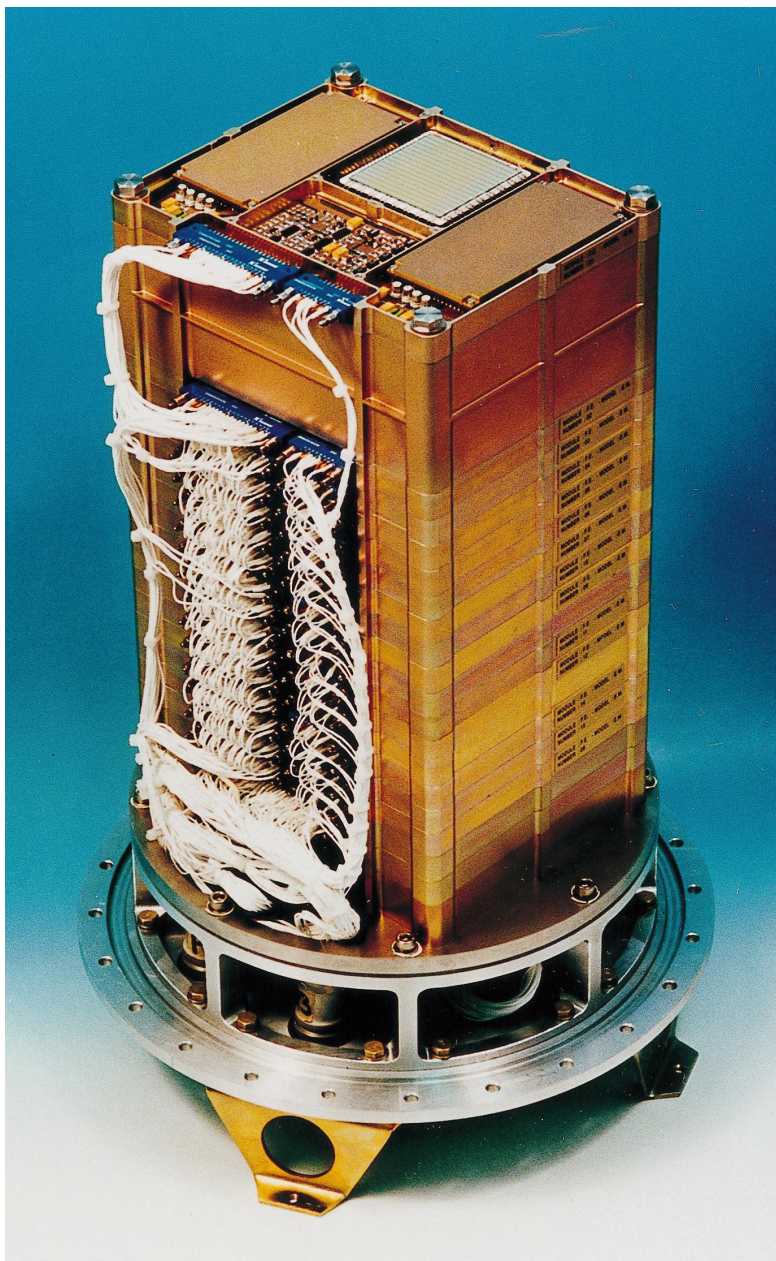


Fig. 2. Box D1.

particle incident angle. The 16 planes are modular, so that mechanically and electronically they are interchangeable. This allows fast modifications, even using parts of the Engineering Model if necessary. Below the 16 active modules, other four cards

are placed, dedicated to the trigger electronics, silicon power supply, analog–digital conversion, FIFO.

The geometric factor of the detector is $8.3 \text{ cm}^2\text{sr}$ for low-energy particles which stop in the second plane, and decreases with increasing energy.

The whole structure is surrounded by a cylindrical aluminum vessel of 284 mm diameter and 480 mm height. The top part is rounded, while in the bottom side the connectors interfacing the other parts of the instrument are located. The vessel is 2 mm thick, except for a little window in correspondence to the first silicon plane where it is reduced to 300 μm ; this choice has been made in order to minimize the amount of passive material the particles cross before reaching the sensitive detector. The cylinder is filled up with nitrogen at 1.2 atm; the pressure will slowly decrease during the years to reach 0.8 atm after 3 yr.

The signal produced by the incoming particles in the silicon strips is amplified and shaped before performing the conversion from analog to digital. Each plane of the telescope has two 16 channels preamplifiers, corresponding to each detector strip.

The analog signal is digitized by means of a 12 bit (4096 channels) ADC. The ADC overflow channel corresponds to 2800 mip, 1 mip being equivalent to 30 400 electrons or 105 keV; the resolution per channel is about 0.68 mip/ch, or 0.07 MeV/ch.

The 512 element (32×16) data matrix is sent after digitization to D2, where all operations of cleaning and filtering of the information are performed. In addition to the scientific data used for particle identification, also housekeeping data (temperatures, rate meters, currents, voltages), monitoring the status of the detector, are delivered to D2.

2.2. Operating modes

NINA can work in different operating conditions, switched automatically or via telecommand, which affect the trigger system. In particular:

1. Two thresholds for the energy deposits in the single silicon layers have been implemented: a low threshold (LT), corresponding to 2.5 mips, and a high threshold (HT), corresponding to 25 mips.

In the first two layers, in order to compensate the smaller thickness, the HT corresponds to 0.48 of the one previously defined; this allows to save the detection of almost all He nuclei.

2. The strips 1 and 16 of every silicon layer, except plane 1, are used as lateral anticoincidence sys-

tem, and are physically connected to the same output.

If the hardware lateral anticoincidence is set off by a dedicated telecommand, a software veto system operates the selection of the tracks not hitting the lateral strips. It is impossible to totally exclude (hardware and software) the lateral anticoincidence.

3. The planes 15 and 16 can be used as bottom anticoincidence. The default operating mode adopts the plane 16 but, in case of failure, the plane 15 can be selected by telecommand.

The bottom anticoincidence can be totally removed (by telecommand), allowing the detection of particles crossing the whole apparatus.

The main trigger of the acquisition system is the following:

$$\text{TRG M1} = D_{1x} \times D_{1y} \times ((D_{2x} + D_{2y}) + (D_{3x} + D_{3y})),$$

where D_{ij} is the above-threshold signal coming from the plane i , view j ($j = x, y$). The logic OR of planes 2 and 3 provides redundancy in case of a failure of plane 2.

In the default operating mode, this trigger is used together with the lateral and bottom anticoincidence ON, in order to ensure the complete containment of the particle inside the detector; this is indeed the condition allowing the best energy and nuclear discrimination in NINA. Moreover, TRG M1 can be used with LT or HT, defining two different intervals of nuclei which can be detected. In particular, TRG M1 together with HT cuts from the trigger most of the protons and a very small percentage of helium (Fig. 3).

Finally, TRG M1 allows a good reconstruction of the particle trajectory.

For particular data taking demands, or in case of failure of the first plane, it is possible to switch, via telecommand, to a second trigger:

$$\text{TRG M2} = (D_{2x} + D_{2y}) \times (D_{3x} + D_{3y}) \times (D_{4x} + D_{4y}) \times (D_{5x} + D_{5y}),$$

which is used again in its basic operating mode with the lateral and bottom AC ON. This trigger increases the acceptance angle, although with

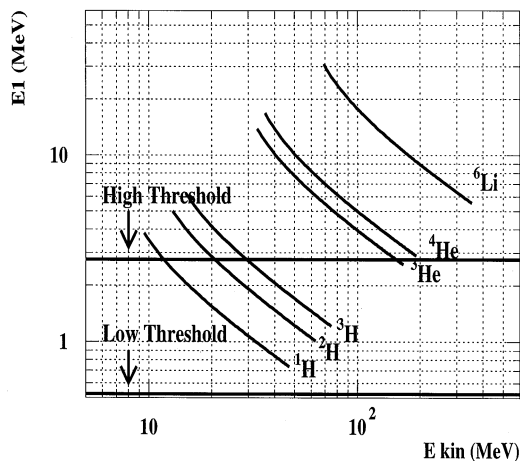


Fig. 3. Effects of the HT and LT on the acquisition of ^1H , ^2H , ^3H , ^3He , ^4He and ^6Li contained in the detector, in case of TRG M1. E_{kin} is the kinetic energy of the incident particle; E_1 is the energy the particle releases in the first plane of NINA.

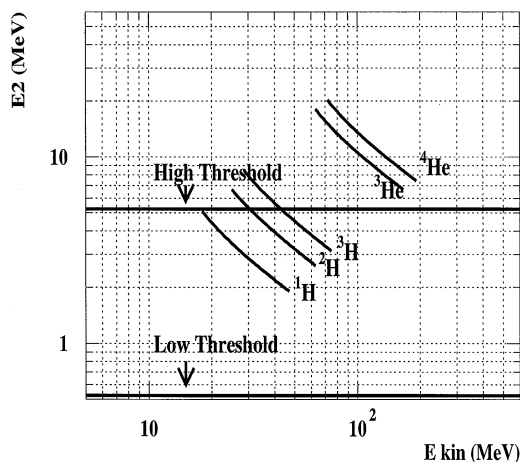


Fig. 4. Effects of the HT and LT on the acquisition of ^1H , ^2H , ^3H , ^3He and ^4He contained in the detector, in case of TRG M2. E_{kin} is the kinetic energy of the incident particle; E_2 is the energy the particle releases in the second plane of NINA.

a worsening of the angular resolution. The combination of TRG M2 and HT excludes most of the protons from the trigger, but keeps all He nuclei (Fig. 4).

The acceptance window of particles with TRG M1, LT and request of full containment of the event

Table 1

Energy windows for the most abundant particles in NINA detector. The default operating mode with TRG M1, LT, bottom and lateral AC ON is selected. E_{min} is the minimum energy for triggering; E_{max} is the maximum energy for the containment

Particle	Z	E_{min} (MeV/n)	E_{max} (MeV/n)
^1H	1	10.0	48.0
^2H	1	6.5	32.0
^3H	1	5.0	25.3
^3He	2	11.0	55.7
^4He	2	9.25	47.2
^6Li	3	11.5	59.3
^7Li	3	10.6	54.4
^7Be	4	14.6	75.1
^9Be	4	12.7	65.2
^{10}B	5	16.0	79.0
^{11}B	5	14.6	74.6
^{12}C	6	17.5	87.5
^{14}N	7	18.6	95.0
^{16}O	8	20.0	103.1
^{19}F	9	21.0	106.8
^{20}Ne	10	23.0	117.0
^{28}Si	14	27.5	141.8
^{40}Ca	20	38.5	174.5
^{56}Fe	26	58.2	194.6

is shown in Table 1. The spectrum of nuclei extends from hydrogen to iron in the energy interval 10–200 MeV/n.

If the bottom anticoincidence is removed, NINA can register nuclei up to 1 GeV/n, still with a good nuclear discrimination.

2.3. Acquisition modes

The maximum amount of data that NINA can send to ground from the satellite varies between 2 and 4 Mbyte/day, out of a total mass memory of 14 Mbytes. Therefore, a limit to the acquisition capability of the instrument has been provided, organizing a system which, at high rate conditions, enables the detector to register events with less detail.

The flux of particles changes notably along the orbit. Every 60 s the processor in D2 calculates the rate of particles reaching the detector, and selects one of the following acquisition modes:

1. *Full-format mode* (counting rate up to 10 Hz).

This mode, in which the whole event topology is recorded, is the normal working configuration

outside the earth radiation belts. It allows to measure the energy released by the particle in each silicon detector (Bragg curve). Within the precision allowed by the strip pitch, we can also reconstruct the particle trajectory, identify its range with good precision and check for multiple tracks and for particles which escape the telescope due to the geometrical inefficiencies of the anticoincidence system.

2. E_1 – E_{tot} mode (counting rate 10–100 Hz). At high fluxes it is necessary to make an optimal use of the mass memory storage. In this acquisition mode a second level trigger, driven by the D2 microprocessor, restricts the event acceptance only to particles crossing the four central strips of the first two planes of the telescope, and leaving a single cluster of fired strips (multiple tracks subtraction). Once these conditions have been fulfilled, the energy E_1 released in the first plane and the energy E_{tot} deposited in the whole detector by the crossing particle are calculated. Instead of the whole event topology, only the E_1 and E_{tot} information of the event (E_2 and E_{tot} in case of TRG M2) is transmitted.
3. *Rate meter mode* (counting rate above 100 Hz). If the trigger rate rises above 100 Hz, only the counting rates of certain planes at different depths of the telescope are read and stored (every 60 s). Two signal integration systems have been implemented, so as to have information both at high and low rates. The scientific information in rate meter mode is obviously strictly reduced, but allows nevertheless to perform a global check of the system and an estimation of the rate of particles inside the radiation belts or in presence of solar flares.

The switching among the different acquisition modes is gradual and can happen only at intervals of 60 s, to avoid oscillations; even if the rate suddenly exceeds 100 Hz, it is necessary to go through the E_1 – E_{tot} mode before reaching the rate meter mode.

2.4. Ground operations

The interaction between the ground station and NINA during the flight is driven by 24 telecommands. Some are dedicated to operations like

power switching ON/OFF, data transferring, memory cleaning, single or dual microprocessor mode setting. The others act on the trigger logic or on the storage model.

TLC's are the only way to communicate with the instrument when in orbit. The transmission of different telecommands can be performed only when the satellite passes over the ground stations. A packet with the status of the telecommands is sent to Earth each time a change has occurred.

As already mentioned, the default telecommand set initializes an event acquisition with the TRG M1, LT, lateral strips and bottom plane in anticoincidence, and acquisition mode automatically switching to the different options, depending on the counting rate. Nevertheless, it is possible to set any combination of trigger logic, threshold level, anticoincidence and acquisition mode by telecommands.

3. Beam test at GSI

In April 1997 the Flight Model was tested at GSI (Gesellschaft für Schwerionenforschung) Laboratory in Darmstadt (Germany), which provided a ^{12}C beam.

For this test, all parts of NINA (boxes D1, D2, P and E) were used in a fully operational mode. The satellite acquisition system and the telemetry transmission were simulated by means of a custom-made instrument (GSE – Ground Support Equipment) which interfaced, by means of Camac modules, the box E to the data acquisition system.

In Fig. 5 the experimental setup in both the control and the beam room is shown. The whole NINA instrument, plus the power supply, the GSE and its PC were placed in the beam room. Two scintillators were put in front of the detector for beam monitoring. The GSE PC was controlled by remote. In the control room were also located electronic modules for processing the scintillator signals and a precision system for moving the box D1 with respect to the beam line.

Data were taken in different runs at the carbon beam energies of 300, 100, 80 and 65 MeV/n. Some measurements were performed interposing a polyethylene target, 0.6 mm thick, between the box D1

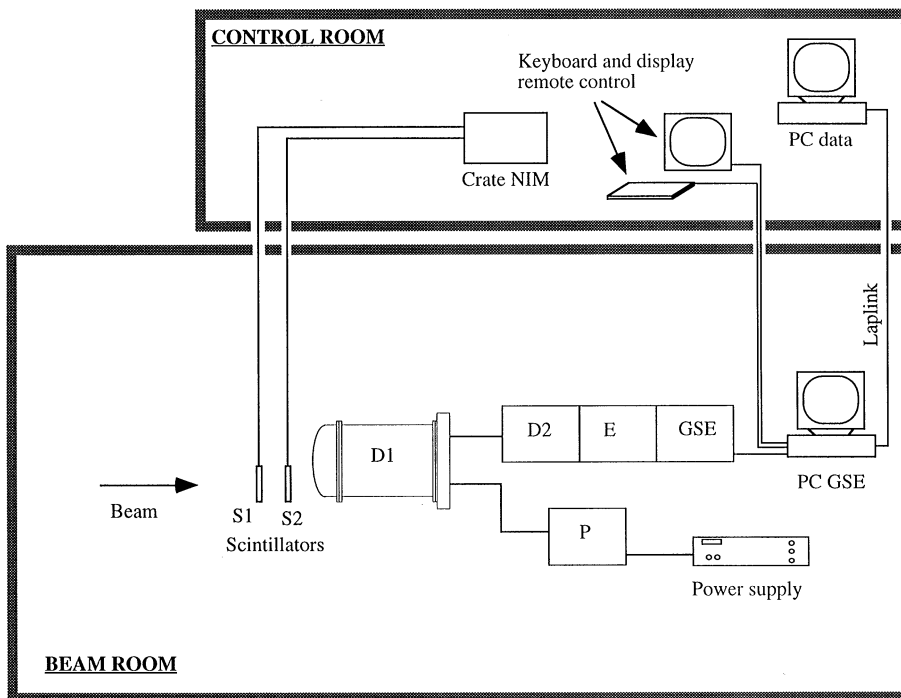


Fig. 5. Sketch of the experimental setup used in April 1997 beam test at GSI.

and the beam, in order to obtain all the products of the ^{12}C fragmentation. In some runs the scintillators were removed in order to have a monochromatic beam.

All possible telecommand settings (triggers, thresholds, lateral and bottom anticoincidences) were tested during this period. Tests of the behavior of the detector as a function of time and temperature were done as well. Most of the runs were performed in Full-Format mode, the remainder in E_1-E_{tot} mode.

3.1. Energy calibration

Two different methods have been used to calibrate energy in the detector. In both procedures, different samples of nuclei from proton to carbon at different energies were extracted from the whole set of GSI data and examined; straight and clean tracks contained in the telescope volume and passing through the central strips of the detector were selected.

In the first method, the detector has been calibrated by comparing the energy deposits of the collected families of nuclei in each silicon view, expressed in ADC channels, with the corresponding simulated ones expressed in MeV. Monte Carlo simulation programs (Geant 3.21 [7]) had been previously calibrated using monochromatic proton and helium beams at the PSI Laboratory of Willigen (Zurich – Switzerland).

From the distribution of the conversion factors (MeV/ADC Ch) in each silicon view and for the various particles at different energies, we obtained the following average ratio between MeV energy and ADC channels:

$$R = (0.067 \pm 0.002) \frac{\text{MeV}}{\text{ADC Ch}}, \quad (1)$$

holding for the whole energy spectrum of the ADC.

The second approach consisted of an interpolation procedure, which fitted a Bragg curve to the energy values released by the nuclei in each silicon

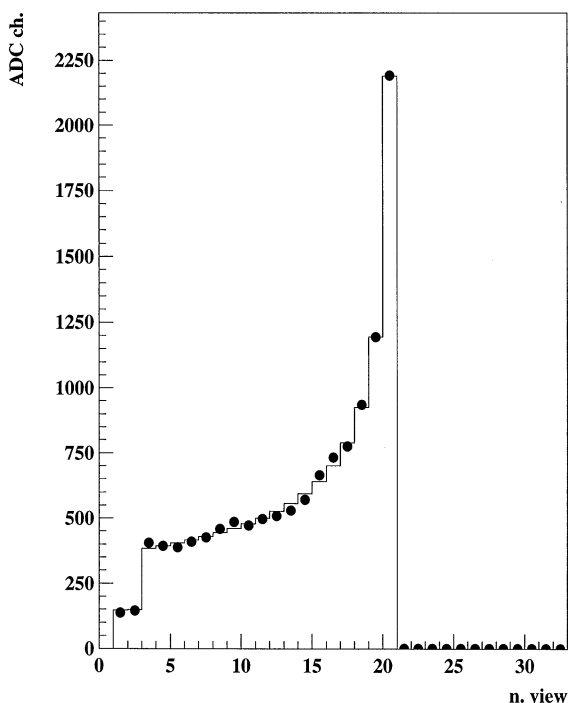


Fig. 6. Best-fit of the Bragg curve of a carbon nucleus, which stopped in the 20th silicon view. The bullets represent the experimental energy losses in each silicon layer.

layer. This curve is based on the Bethe–Bloch formula, which depends on the kinetic energy, the atomic and the mass number of the nuclei. We kept these quantities fixed in the fit allowing only the additional parameter of conversion between MeV and ADC counts to change.

In Fig. 6 the best-fit of a Bragg curve of a carbon nucleus is shown; the bullets represent the experimental energy deposits in each silicon view. Fig. 7 represents instead the distribution of the calibration factors as determined by a fit of a sample of carbon events; mean value and standard deviation are estimated by a Gaussian fit of the histogram.

The results of this procedure, applied to different particles with different kinetic energy, are in agreement within the errors with the ones coming from the former method.

Fig. 8 shows the E_1 vs. E_{tot} curves of real particles, coming from the fragmentation of the original carbon beam by means of the polyethylene target, with energies expressed in MeV. All the products of fragmentation are visible, and the en-

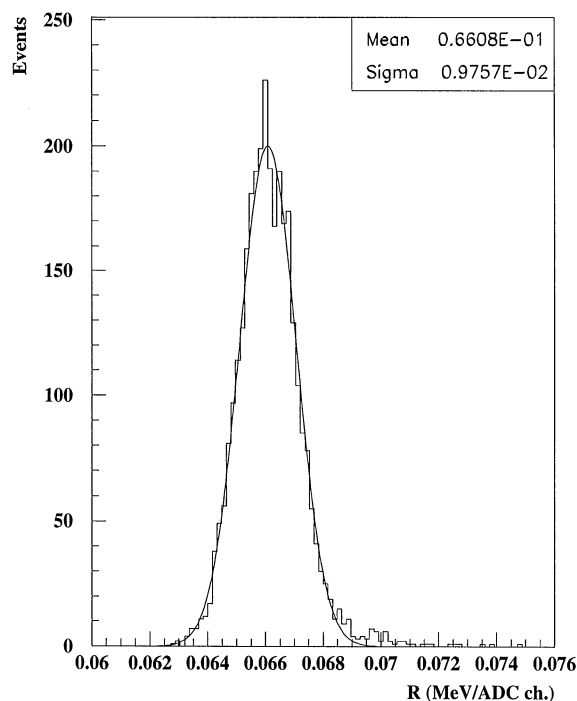


Fig. 7. Distribution of the calibration factors coming from best-fits of a sample of carbon events, fitted by a Gaussian curve.

ergy behavior is in good agreement with the expected simulated data [4].

3.2. Mass analysis

The full-format acquisition mode allows the complete registration of the particle track with all its energy deposits in the strips; in this condition, therefore, the best nuclear and isotope discrimination can be performed.

The nuclear families coming from the fragmentation of the ^{12}C beam are well separated by the E_1 vs. E_{tot} technique (Fig. 8). This separation of groups of equal Z is better visualized by using the product of the E_1 and E_{tot} deposits, as shown in Fig. 9 for the same sample of GSI data.

Once the charge has been identified, the mass M of the specific isotope can be reconstructed by means of the equation:

$$M = \left(\frac{a(E^b - (E - \Delta E)^b)}{Z^2 \Delta x} \right)^{1/(b-1)}, \quad (2)$$

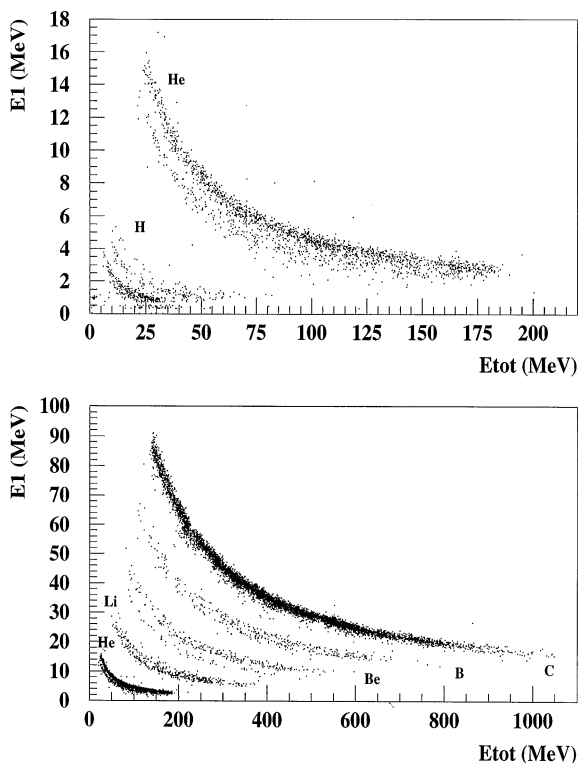


Fig. 8. Distribution of the energy released in the first plane (E_1) and total energy (E_{tot}) detected for particles produced in the fragmentation of ^{12}C at GSI.

where ΔE is the energy lost by the particle in a thickness Δx measured starting from the first plane. This algorithm of mass reconstruction is well known in literature [8,9] and adopted in many experiments [10].

The parameter a is a constant of the medium while b has a value between 1.5 and 1.8 in NINA's energy range. A precise evaluation of such parameters for each atomic species has been obtained by a fit of the following expression:

$$R = a \frac{M}{Z^2} \left(\frac{E}{M} \right)^b, \quad (3)$$

where R and E are respectively the measured range and the kinetic energy of known particles of mass M and charge Z . From simulations it turned out that a and b do not have a strong dependence on the mass of the isotope, therefore a mean value for each Z can be taken. The procedure of fitting has

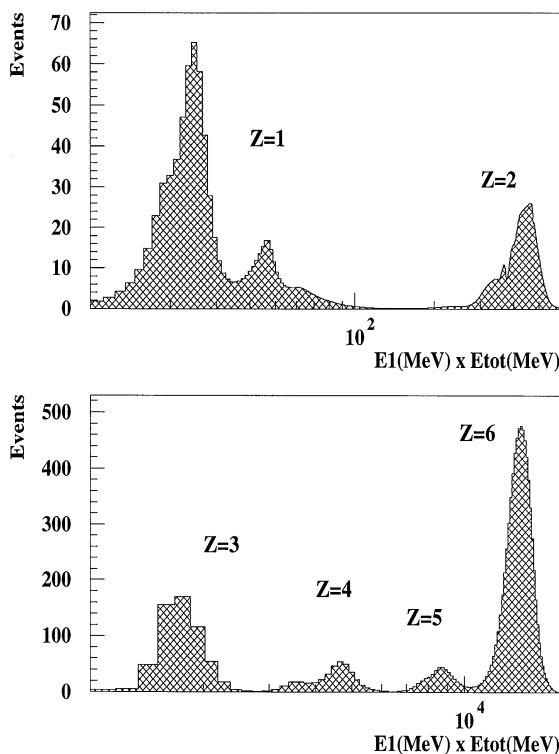


Fig. 9. Distribution of the energy released in the first plane (E_1) multiplied by the energy released in the whole detector (E_{tot}) for particles coming from fragmentation of ^{12}C , produced at GSI.

been done for simulated and experimental GSI data, and the two sets of a and b parameters resulted in good agreement.

An important point using expression (2) is the choice of the thickness Δx where to compute ΔE , which corresponds in NINA to a certain number Δn of silicon views hit by the particle. Table 2 presents a list of reconstructed masses with their RMS, using expression (2), as a function of increasing Δx (Δn), for simulated helium and nitrogen at a fixed range. It is evident that the RMS decreases on increasing the number of views taken to compute Δx ; nevertheless there is not a fixed rule for computing Δx , and the choice has to be made according to the range of the particle.

Once the parameters a and b are evaluated and examined for every particle the best option for Δx (Δn), we reconstructed all isotope masses starting from $Z = 1$ to 6, as shown in Figs. 10 and 11.

Table 2

Reconstructed masses by Eq. (2) with their RMS as a function of the number Δn of hit views used to compute Δx , for simulated nuclei (^4He and ^{14}N) stopping at the 15th view

Δn	^4He (3727)	^{14}N (13044)
1	3450 ± 300	12200 ± 550
2	3600 ± 250	12700 ± 400
3	3600 ± 150	12700 ± 250
4	3650 ± 100	12850 ± 200
5	3650 ± 100	12850 ± 150
6	3700 ± 90	12950 ± 150
7	3690 ± 80	12900 ± 150
8	3710 ± 70	12950 ± 100
9	3720 ± 70	12950 ± 100
10	3730 ± 60	13000 ± 100
11	3740 ± 60	13000 ± 100
12	3750 ± 50	13000 ± 100
14	3780 ± 50	13000 ± 100

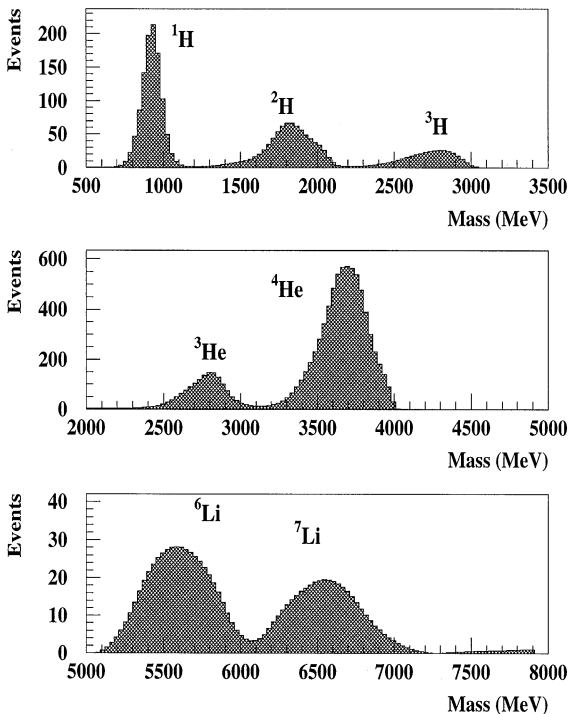


Fig. 10. Distributions of the masses reconstructed by Eq. (2) for events of $Z = 1, 2$ and 3 collected at GSI.

The incident direction of the particle has been taken into account. For every mass, a Gaussian fit has been performed, evaluating in such a way the average value of the reconstructed mass M and its

corresponding standard deviation σ . The results of this analysis are summarized in Table 3, for all isotopes studied.

Results up to carbon give sigmas of about 0.3 amu. Such results confirm the good capability of this instrument to perform isotope analysis.

The total statistics collected during the test was too scarce to allow a clear observation of very rare isotopes. For instance, pictures referred to lithium have a tail around 7500 MeV, which could have been attributed to ^8Li . For carbon, the long tail towards smaller masses can reasonably belong to nuclei of ^{11}C .

An alternative approach for nuclear and isotopic discrimination in NINA, based on the Artificial Neural Network (ANNs) computational paradigm, is under investigation. ANNs have been used by this collaboration for particle [11,12] and energy classification [13] in detectors for cosmic rays. Their discrimination capability on simulated light nuclei in NINA detector has already been studied

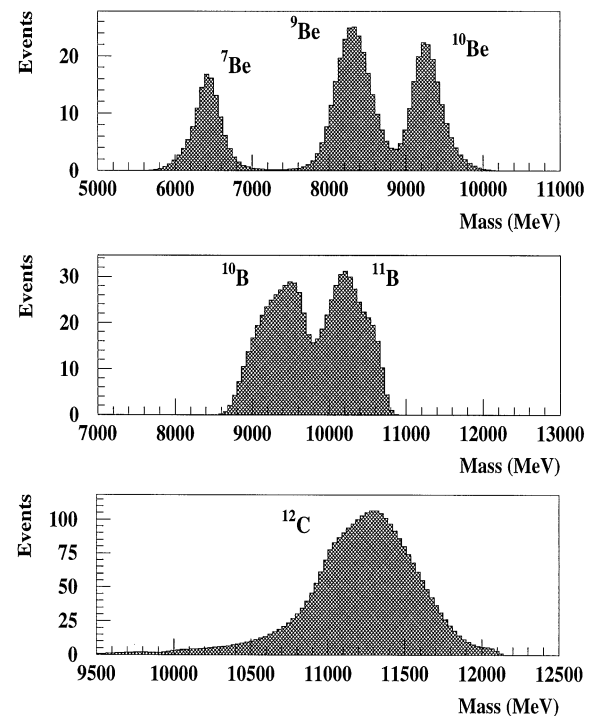


Fig. 11. Distributions of the masses reconstructed by Eq. (2) for events of $Z = 4, 5$ and 6 collected at GSI.

Table 3

Mean values M and standard deviations σ from the Gaussian fits of the masses reconstructed by Eq. (2), for events collected at GSI

Z	Isotope, M (MeV)	\overline{M} (MeV)	σ (MeV)	σ (amu)
1	^1H , 938	939	67	0.072
1	^2H , 1875	1834	153	0.164
1	^3H , 2814	2761	191	0.205
2	^3He , 2814	2828	146	0.157
2	^4He , 3727	3742	155	0.167
3	^6Li , 5603	5589	154	0.165
3	^7Li , 6535	6545	208	0.223
4	^7Be , 6536	6504	214	0.230
4	^9Be , 8394	8409	237	0.254
4	^{10}Be , 9328	9359	206	0.222
5	^{10}B , 9327	9278	282	0.303
5	^{11}B , 10255	10170	290	0.311
6	^{12}C , 11178	11239	279	0.300

[14]. At present, an extension of this work to include also real data is in progress, and the corresponding results will be published elsewhere.

4. Conclusions

The Flight Model of the telescope NINA has been calibrated at GSI Laboratory in April 1997 and is now integrated on the satellite Resource-01 version n.4. The launch from the basis of Baikonur in Kazakhstan is fixed for June 1998.

Results coming from beam tests, aiming to estimate the mass discrimination capability of the instrument, have been examined in detail and reported in this article. As final result, the different isotope species can be discriminated by NINA with

sigmas of the reconstructed masses less than 0.3 amu, at least up to $Z = 6$.

Acknowledgements

We acknowledge the Laben company (Italy) for the realization of D1 and D2 parts of the detector, as well as VNIIEM (Russia) for parts E, P and especially for all the operations related to Resource satellite. We also would like to thank all the INFN technical staff and all people at GSI Laboratory for their kind cooperation.

Finally we acknowledge the State Committee of Science and Technology of the Russian Federation, who partially supported this work.

References

- [1] V. Bidoli et al., Nucl. Instr. and Meth. A 399 (1997) 477.
- [2] O. Adriani et al., Proc. XXV ICRC, Durban, 1997, vol. 5, p. 49.
- [3] G. Barbiellini et al., Nucl. Instr. and Meth. A 354 (1995) 547.
- [4] A. Bakaldin et al., Astroparticle Phys. 8 (1997) 109.
- [5] F. Aversa et al., Nucl. Instr. and Meth. A 360 (1995) 17.
- [6] M. Bocciolini et al., Nucl. Instr. and Meth. A 370 (1996) 403.
- [7] Geant, Detector Description and Simulation Tool, CERN Geneva, Switzerland.
- [8] F.S. Goulding, Nucl. Instr. and Meth. A 162 (1979) 609.
- [9] N. Hasebe et al., Nucl. Instr. and Meth. A 325 (1993) 335.
- [10] D.N. Baker et al., IEEE Trans. Geosci. Remote Sensing 31 (3) (1993) 531.
- [11] R. Bellotti et al., Astroparticle Phys. 7 (1997) 219.
- [12] M. Casolino et al., Nucl. Instr. and Meth. A 360 (1995) 371.
- [13] R. Borisyuk et al., Nucl. Instr. and Meth. A 381 (1996) 512.
- [14] M. Ambriola et al., Nucl. Instr. and Meth. A 443 (1998), to be published.